Energy
Advances

Ar/N$_2$

Carbon Electrode

Perovskite Absorber

Mesoporous Titanium Oxide

Fluorine Tin Oxide

Ambient

ROYAL SOCIETY
OF CHEMISTRY

PAPER
Subhendu K. Panda *et al.*
An ambient process for hole transport layer-free highly
stable MAPbI$_3$ by addition of MACl for efficient perovskite
solar cells

PAPER

Check for updates

An ambient process for hole transport layer-free highly stable MAPbI₃ by addition of MACl for efficient perovskite solar cells†

Pardhasaradhi Nandigana, [ID] [ab] Bavatharini Saminathan, [a] Sriram P., [ab] Sujatha D., [ab] Imthiaz Ahmed M., [a] Ram Prasanth R., [a] B. Subramanian[ab] and Subhendu K. Panda [ID] ★[ab]

Methylammonium lead iodide (MAPbI₃) is a front-runner material for efficient perovskite solar cells (PSCs) due to its high light-absorption coefficient, suitable bandgap, and superior charge carrier mobility. However, high-quality photoactive MAPbI₃ (MAPI) perovskite thin-films are usually fabricated in controlled atmospheric conditions (inside a glove box) and annealed at high temperature (generally >120 °C for 20 min). Here, we report a facile method to fabricate high quality MAPbI₃ (MAPI) thin-films by the simple addition of an MA-based volatile additive, *i.e.*, methylammonium chloride (MACl). The optimized amount of MACl in the perovskite solution produced a highly crystalline and optically active MAPI black perovskite phase at room temperature under ambient atmospheric conditions. MACl not only regulates the surface morphology of the perovskite films, but also the intermediate phases by altering the formation energy of the perovskite material. MACl lowered the formation energy of the MAPI perovskite resulting in the room temperature formation of phase pure MAPI perovskite under ambient conditions. Finally, we assembled perovskite solar cell devices with an HTL-free carbon-based architecture to determine the photovoltaic performance of the prepared thin-films. Our champion device showed a power conversion efficiency as high as 7.11% with an open circuit voltage of 0.98 V, short circuit current density of 11.03 mA cm^{-2} and a fill-factor of 65.86%. The device was stable over 10 days under ambient conditions and retained ∼80% of its initial efficiency. These results are favourable for large-scale fabrication to make it commercially viable.

Introduction

In recent years, hybrid organic–inorganic metal halide perovskites (AMX₃: A = organic cation, M: Pb and X: halide (I, Br, Cl)) have gained great attention due to their excellent optoelectronic properties, such as high charge carrier mobility, tunable band gap, small exciton binding energy, long carrier diffusion length, and high absorption coefficients.[1–4] Miyasaka and co-workers utilized perovskite (MAPbI₃/MAPbBr₃) nanocrystals as a light absorber material in dye sensitized solar cells (DSSCs) for the first time and reported that the power conversion efficiency (PCE) was about 3.8% in 2009.[5] In 2012, Park and Gratzel et al. introduced a solid hole transport layer in perovskite solar cells to enhance the stability and performance of the device.[6]

The power conversion efficiency (PCE) of single junction perovskite solar cells (PSCs) has been increased to over 25.7% surpassing the record of conventional silicon-based solar cells.[7] Currently, most of the perovskite solar cell fabrication is confined to a controlled atmosphere (N₂/Ar filled glove box) and annealing at high temperatures such as 130 °C to 150 °C to form the perovskite phase. These conditions will limit the production of perovskite solar cells on an industrial scale. It's necessary to fabricate the solar cell devices under ambient conditions at room temperature to make it commercially viable. Wan-Jian Yin *et al.* reported a dramatic decrease in the formation temperature of CsPbI₃ perovskite thin-films by the incorporation of small amounts of bromide.[8] Similarly, Dianyi Liu and co-workers continued this work and fabricated CsPbI₂Br perovskite thin-films at room temperature showing a PCE of 8.67% for flexible inverted PSCs.[9] Maryam Bari and co-workers reported room temperature grown MAPbX₃ (X = I, Br, Cl) single crystals by creating constant supersaturation during the crystal growth and obtained large single crystals at room temperature *via* controlled solvent evaporation and studied their optical

[a] *EMF Division, CSIR – Central Electrochemical Research Institute, Karaikudi, Tamil Nadu 630003, India. E-mail: skpanda@cecri.res.in; Tel: +91 4565 241234*

[b] *Academy of Scientific and Innovative Research (AcSIR), Ghaziabad-201002, India*

† Electronic supplementary information (ESI) available. See DOI: https://doi.org/10.1039/d3ya00500c

properties.[10] Lixiu Zhang *et al.* reported room temperature formation of MAPI perovskite thin-films by using a low boiling point solvent and obtained a PCE of 18.21%.[11] Zijiang Yang and co-workers developed a novel strategy to produce the room temperature formation of phase pure MAPI perovskite thin-films *via* anti-solvent (chloroform) washing and reported a PCE as high as 17.7% under ambient conditions with a relative humidity of about 30% at room temperature.[12] To form a highly crystalline iodide or iodide/bromide perovskite and attain high performance in PSCs, sources containing only iodide and bromide salts (such as PbI_2, $PbBr_2$, MAI, FAI, CsI, MABr) are typically used as precursors. However, recently, MACl as an excellent additive to regulate the perovskite crystallization, giving uniform film formation (full coverage over all the surface of the perovskite thin-film) and defect passivation at grain boundaries in the presence of MACl, has been widely explored.[13–15] Zhu *et al.* introduced MACl in the bulk MAPI perovskites for the first time and studied their crystal structure, charge carrier dynamics and performance of PSCs. They observed better film formation and improved recombination resistance in planar perovskites, which results in an enhanced PCE from 2% to 12%.[15] Besides, there are different ways to introduce MACl effectively into the bulk perovskites, such as one-step conventional spin-coating, one-step spin-coating under iodide-deficient conditions, two-step conversion, and post-treatment of the perovskite film with MACl.[16–19] Among these routes, a single step deposition process, *i.e.* addition of an excess amount of MACl to the 1:1 ratio of MAI and PbI_2 resulted in higher crystallinity, and good morphology with higher grain size and entire surface coverage without pinholes on the perovskite thin-films was observed, which resulted in enhanced performance of the PSC with negligible hysteresis.

It is important to mention that MACl not only regulates the surface morphology of the perovskite films, but also regulates the intermediate phases of the perovskite material at the time of deposition. Kim and co-workers investigated the effect of MACl on the perovskites ($FAPbI_3$) experimentally as well as theoretically. MACl successfully induces the intermediate phase of pure α-$FAPbI_3$ at room temperature. Furthermore, the formation energy of the bulk perovskite varies with the concentration of MACl incorporated into the perovskite solution.[20] The formation energy of MAPI is less than that of $FAPbI_3$ because the ionic radius of the MA cation is less than that of the FA cation. In this work, we are incorporating an optimized amount of MACl into the MAPI perovskite solution (PbI_2:MAI with 1:1) for room temperature formation of phase pure semiconductor grade MAPI perovskite films. MACl modified MAPI films showed high crystallinity, improved surface morphology with larger grain sizes and improved optoelectronic properties at room temperature under ambient conditions. To promote commercialization, lowering the production cost and reducing the complexity of the process would make the devices more competitive and thus are highly required. In this respect, we assembled perovskite solar cell devices with a HTL-free carbon-based device architecture (FTO/c-TiO_2/mp-TiO_2/perovskite/carbon) and studied their photovoltaic properties and stability under ambient atmospheric conditions.

Experimental section

Materials

Methylammonium iodide (MAI) (99.0%), lead iodide (PbI_2) (99.99%), and methylammonium chloride (MACl) (98.0%) were purchased from TCI chemicals. Chlorobenzene (Extra Pure), DMF (99%) and DMSO (99.9%) were purchased from Alfa Aesar. Titanium oxide nanoparticles (P-25) (99.5%), titanium(IV) iso-propoxide (98%), conductive carbon paste and FTO glass substrates (7 Ω sq^{-1}) were purchased from Sigma Aldrich. Absolute ethanol (100%, Hayman ethanol) was used. All the chemicals were used without further purification.

Perovskite thin-film fabrication

Perovskite solution was prepared by mixing equimolar (1.3 M) amounts of MAI and PbI_2 in DMF and DMSO mixed solvent (7:3) and stirred overnight. The obtained clear perovskite solution was used for spin coating. Then the perovskite thin-films were prepared by spin coating by a two-step spin coating process. Initially, 40 μL of the perovskite solution was drop cast onto FTO and spin coated at 1000 rpm for 10 s, followed by 5000 rpm for 30 s. During the second step, the anti-solvent chlorobenzene was dropped 10 s before completion. Pristine perovskite thin-films without annealing were named as MAPI_RT, and the films annealed at 120 °C were named as MAPI_120 °C. Furthermore, to understand the effect of MACl, different amounts, such as 0.1 M, 0.2 M and 0.3 M of MACl were added to the pristine perovskite solutions and stirred for 6 h at room temperature under ambient conditions. The thin-films are fabricated following the same procedure as discussed earlier. Interestingly, the MACl-added perovskite solutions formed highly crystalline, optically active perovskite phases under ambient conditions. A video was taken during the thin-film formation of the black perovskite phase, which is provided in the ESI.† The samples were named MAPI_MACl_1, MAPI_MACl_2 and MAPI_MACl_3 for 0.1 M, 0.2 M and 0.3 M MACl added, respectively. The MACl added perovskite thin-films are used for characterization and device fabrication without further annealing.

Solar cell device fabrication

A fluorine doped tin oxide (FTO) glass substrate with 7 Ω sq^{-1} was used for the fabrication of solar cell devices. The substrates were cleaned using soap solution followed by ultrasonication with DI water, acetone and isopropyl alcohol each for 15 min, respectively. These substrates were dried with N_2 flow and finally treated with oxygen plasma for 15 min. A compact-TiO_2 (c-TiO_2) layer was spin coated onto FTO at 2000 rpm for 30 s and fired at 450 °C for 30 min. c-TiO_2 solution can be prepared by mixing titanium isopropoxide (75 μL) with absolute ethanol (5 mL) and stirred for 1 h and 200 μL of the solution is taken for spin-coating. Furthermore, mesoporous-TiO_2 (mp-TiO_2) was spin coated onto the FTO/c-TiO_2 substrate at 3000 rpm for 30 s and fired at 450 °C for 30 min. mp-TiO_2 was prepared by taking an appropriate amount of TiO_2 (P-25) powder and mixing with organic binders (PEG and PEO) and

stirred overnight. Then, the perovskite layers were coated onto the FTO/c-TiO$_2$/mp-TiO$_2$ as discussed earlier. Finally, commercially available conductive carbon paste (purchased from Sigma) was used as a back contact for the solar cells. The active area of the cell was measured to be 0.09 cm^2. Device fabrication was done at room temperature (27–30 °C) under ambient conditions with a relative humidity of approximately 50–60%.

Characterization and device measurements

Powder X-ray diffraction analysis was carried out using Rigaku, smart lab guidance model at the scan rate of 3° min^{-1}. The surface morphology of the prepared perovskite thin-films captured from field-emission scanning electron microscope (FESEM, Gemini, Supra55VP Zeiss) and the elemental composition of the samples was estimated by using energy dispersive spectroscopy (Quanta 250FEG) attached with SEM. XPS analysis was done using a Thermo Scientific ESCALAB 250XI base system to understand the oxidation states of elements present in the thin-films. The absorbance studies were carried out using a UV-Vis spectrophotometer (Cary 60 UV-Vis Agilent Technologies). Steady state photoluminescence spectra of the prepared thin-films were taken by using a fluorescence spectrophotometer (Flurolog-3, Horiba) and the 565 nm excitation wavelength is for the PL measurements. Time resolved photoluminescence decay measurements were carried out by using DeltaHub equipped with Nano-LEDs (Pulsed diode controller, Horiba), where N-390 nm NanoLED was used as an excitation source. The I–V characteristics of the device were measured using BioLogic (SP-150) equipped with EC-Lab software and measured for both the forward scan (FS) and reverse scan (RS). These measurements were carried out using a solar simulator (Sciencetech-SLB300B) equipped with a visible light filter (AM 1.5G) with 100 mW cm^{-2} intensity (1 sun illumination) calibrated using a reference silicon solar cell (VLSI Standard).

Results and discussion

Fig. 1 shows the schematic representation of MAPI perovskite thin-film fabrication, in which the MAPI film containing MACl formed a phase pure perovskite film at room temperature. In contrast, pristine MAPI films at room temperature showed different intermediate phases. Typically, the formation of pure MAPI perovskite phases requires 120 °C for ~20 min, which was observed from Fig. 1. The formation of phase pure MAPI perovskite thin-films at room temperature is due to the addition of MACl into the perovskite solution. As we know, MACl induces the intermediate phase of pure α-FAPbI$_3$ (FAPI) at room temperature by regulating the formation energy of the bulk perovskite. The formation energy of MAPI is much lower than that of FAPI and further addition of MACl helps to reduce the formation energy of MAPI bulk perovskite which results in the room temperature formation of optically active phase pure perovskite thin-films under ambient conditions.[20] Besides, antisolvent (chlorobenzene) plays a major role while fabricating the perovskite thin-films. Antisolvent treatment can increase the nucleus density during film formation to produce highly crystalline, uniform and pinhole-free perovskite thin-films, which facilitates improved solar cell efficiency, and stability of the device.

Fig. 2 shows the XRD patterns of all the prepared perovskite samples. The diffraction patterns of MAPI_RT film showed multiple peaks indicating intermediate phases.[21] Also, a poor perovskite phase can be observed along with the PbI$_2$ peak (Fig. 2a). In contrast, the MAPI_120 °C film showed a highly crystalline and phase pure perovskite. Fig. 2b demonstrates that all perovskite films exhibit characteristic diffraction peaks at 2θ = 14.0° and 28.4° corresponding to the planes (110) and (220), respectively. Which indicates the complete conversion of the precursor solutions to MAPI perovskite. The peak intensity of MACl added films was observed to be higher than that of pristine MAPI_120 °C. Fig. S1 (in ESI†) shows the intensity comparison of MAPI_120 °C along with the target film MAPI_MACl_1, where it is approximately 14.5 times higher for the later sample. This demonstrates the increased crystallinity and phase purity with the addition of MACl at room temperature under ambient conditions.[22] However, the diffraction peak intensity is gradually reducing while increasing the concentration of MACl
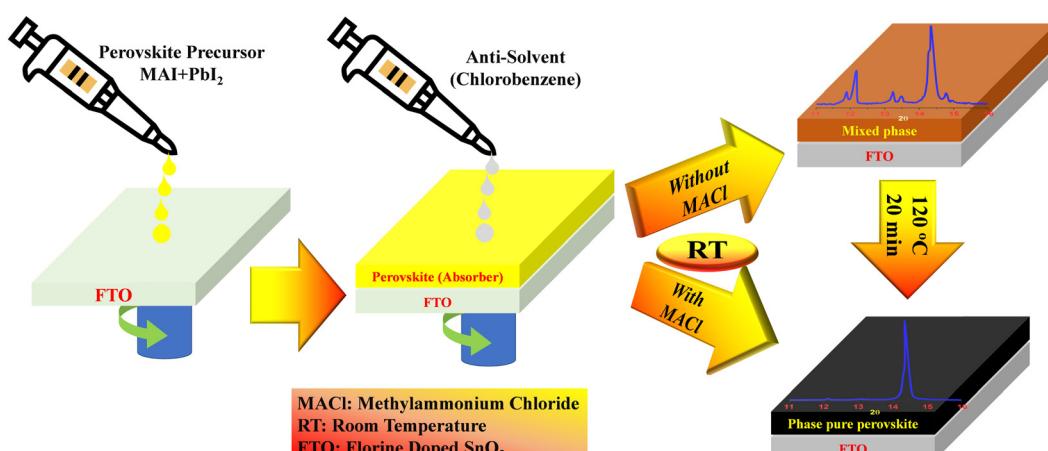
Fig. 1 Schematic representation of room temperature formation of MAPbI$_3$ perovskite thin-films with the addition of MACl under ambient conditions.
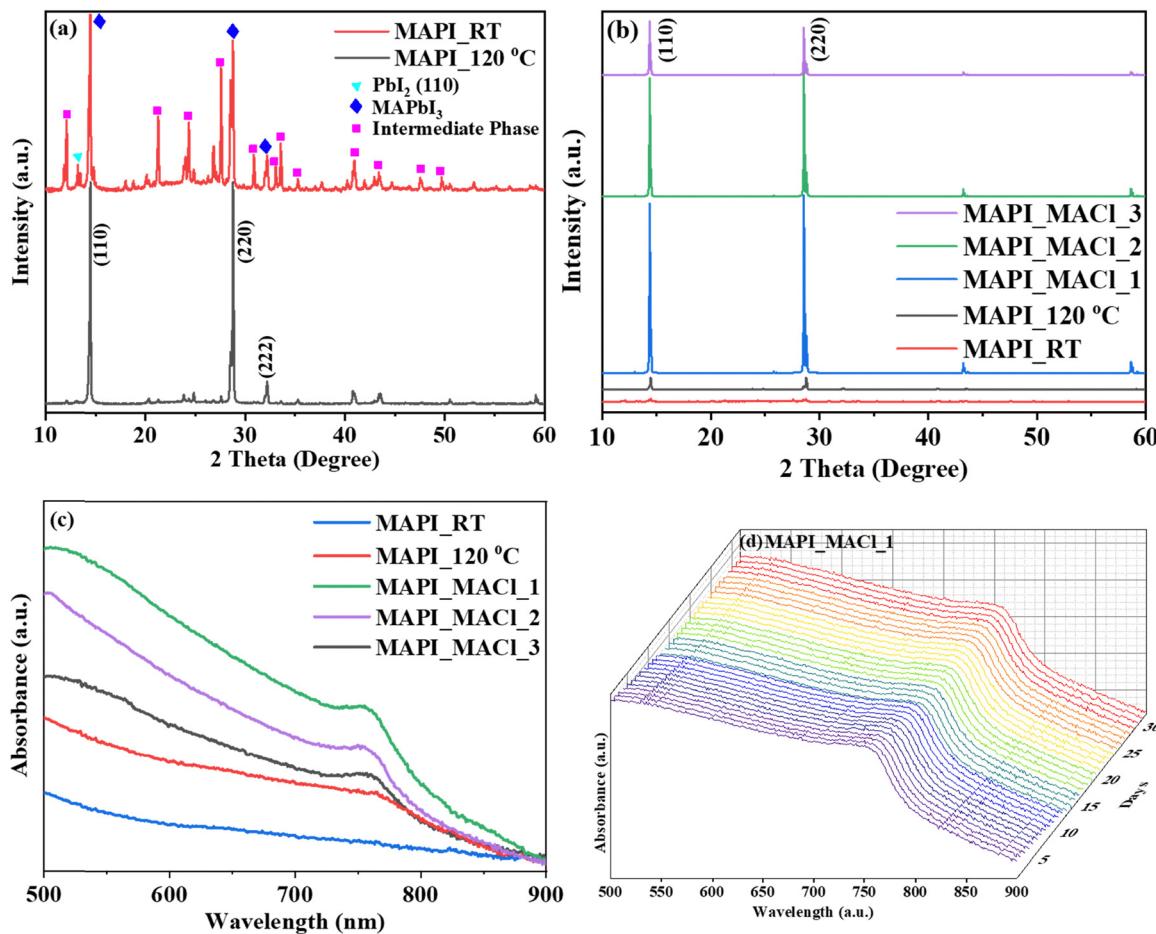
Fig. 2 (a) X-Ray diffraction pattern of MAPI thin-films prepared at room temperature and annealed at 120 °C, (b) XRD patterns of MACl added perovskite thin-films. (c) UV-Vis spectra of prepared perovskite thin-films with different molar amounts of MACl and (d) UV-Vis spectra of MAPI_MACl_1 for 32 days stored under ambient conditions at room temperature.

(Fig. 2b). The excessive amount of MACl in the perovskite film will result in the shrinkage of the perovskite crystals resulting in the reduced diffraction peak intensities.[23]

UV-visible absorption spectroscopy analysis was performed for all the prepared perovskite thin-films to understand their optical properties and the results are shown in Fig. 2c. It can be observed that the MAPI_RT thin-film shows no absorption in the visible region, but the film annealed at 120 °C shows the absorption edge starting from 790 nm and it absorbs light in the entire visible region. Interestingly, the MACl modified MAPI perovskite thin-films showed strong absorption in the same region and the intensity of the MAPI_MACl_1 film was observed to be higher than that of other perovskite films. There is no peak shift observed with the addition of MACl into the MAPI perovskites. Typically, there will be a peak shift towards the blue region for the mixed halide perovskites. Our results show that there is no peak shift, which may be due to the low content of Cl, indicating that Cl-ions are not replacing the I-ions during perovskite film formation. As we know, MACl is a volatile additive, so it will evaporate easily and regulate the perovskite film morphology and formation energy, which results in the room temperature formation of a phase pure and highly

crystalline optically active perovskite phase under ambient conditions.[20] Furthermore, we have calculated the optical bandgap of the thin-films by using a Tauc plot. It is observed from Fig. S2 (ESI†) that all the samples showed a band gap of $\sim$1.53 eV. It has been reported that the organic–inorganic halide perovskites are unstable under ambient, high humidity and high temperature conditions, so it is necessary to examine the stability of the fabricated perovskite thin-films under ambient conditions for a longer period. Hence, UV-Vis absorption measurements for the target sample (MAPI_MACl_1) were studied for over 32 days (Fig. 2d). There is no peak shift or noticeable change in the optical profile observed, which indicates the high optical stability under ambient conditions without any observable degradation.

Another important characteristic of perovskite thin-films is the surface morphology. Fig. 3 shows the surface morphology of the prepared perovskite thin-films. MAPI_120 °C film shows uniform grains with full surface coverage and the size of the grains is around 200–250 nm. The volatile additives MACl generally control the surface morphology resulting in large grain boundaries.[20,22] The MAPI_MACl_1 film shows better surface morphology with an increased grain size of about
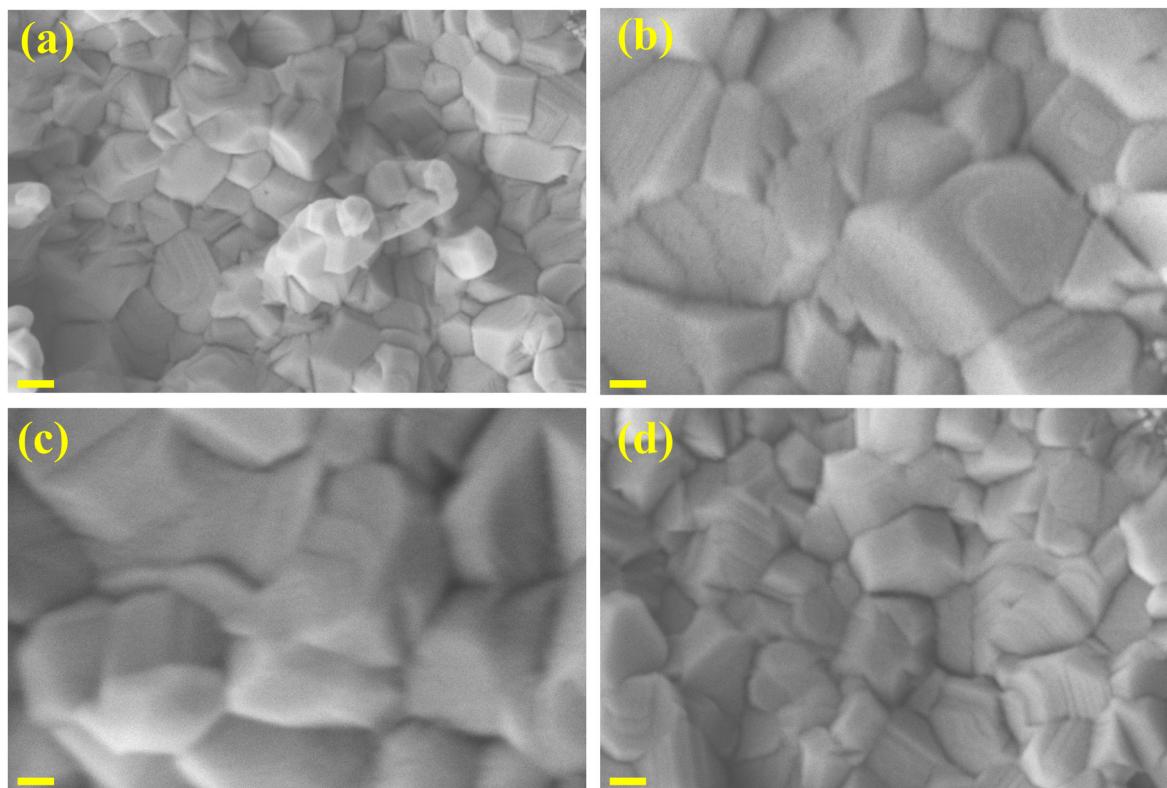
Fig. 3 Scanning electron microscope images of the prepared perovskite thin-films (a) MAPI_120 °C, (b) MAPI_MACl_1, (c) MAPI_MACl_2 and (d) MAPI_MACl_3 (scale bar is 200 nm for all the images).

400 to 500 nm, which is double that of the pristine MAPI_120 °C thin-films. Similarly, the MAPI_MACl_2 film also shows better film morphology with the grain size around 300–400 nm. But in the case of MAPI_MACl_3 the grain size is reduced to ∼300 to 350 nm, which is due to the excess amount of MACl leading to shrinkage in the perovskite crystal
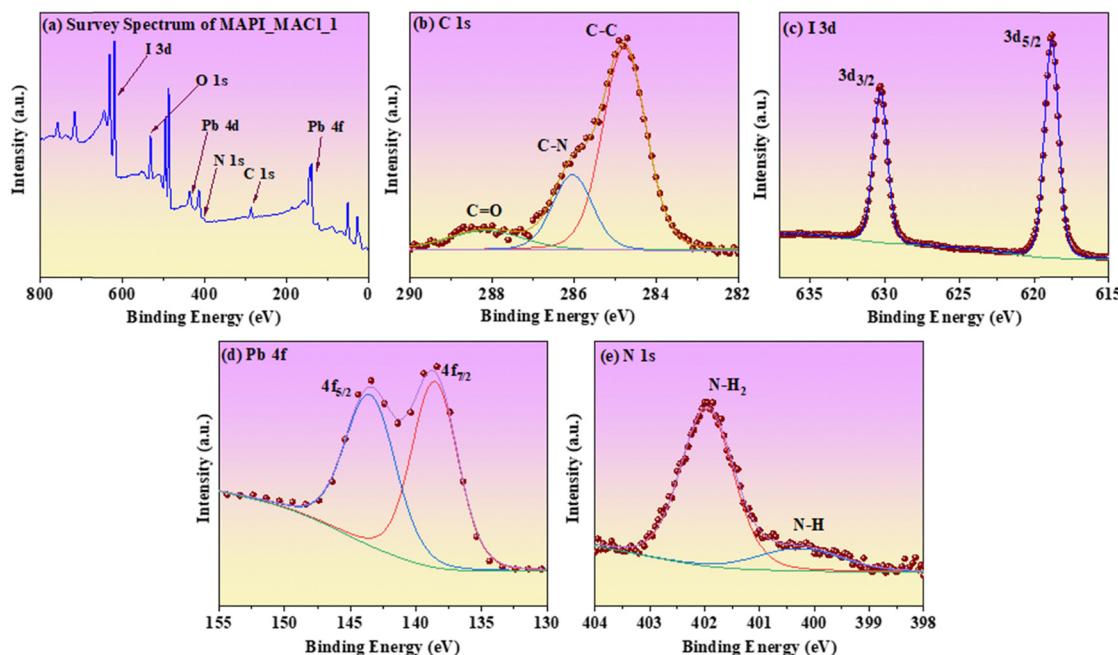

Fig. 4 (a) XPS survey spectrum of MAPI_MACl_1 and (b)–(e) high-resolution spectra of C 1s, I 3d, N 1s and Pb 4f, respectively.

formation resulting in a reduced grain size.[23] Elemental analysis was conducted by EDAX spectroscopy to understand the elemental composition of the prepared perovskite sample (MAPI_MACl_1) and the result is presented in Fig. S3 (ESI†). All the elements are present in their stoichiometric ratio and there is no chlorine content observed in the sample,[22] which agreed with the UV-Vis data.

XPS analysis was performed to understand the chemical composition and oxidation states of the perovskite films and Fig. 4 shows the spectra of sample MAPI_MACl_1. The survey spectrum is shown in Fig. 4a, and it can be observed that all the elements are present and there is no chlorine peak present in the sample, which is further evidence for the UV-Vis spectra (no change in the bandgap even after adding MACl into the perovskite solution).[20] Fig. 4b shows the high-resolution spectrum of C 1s that can be de-convoluted into 3 peaks starting from 284.8 eV, 286 eV and 288.2 eV. In particular, the peaks at 284.8 eV and 286 eV attributed to the sp^2 carbon (C–C) from the surface adsorbed species and carbon bonded with nitrogen (C–C) from the surface adsorbed species and carbon bonded with nitrogen (C–N) in the perovskite organic core respectively. The peak at 288.2 eV assigned to the carbon singly bonded with oxygen (C–O), which is also attributed to surface contamination.[24,25] High-resolution XPS spectra of I 3d are shown in Fig. 4c, and it can be observed that there are strong peaks at 618.8 eV and 630.3 eV attributed to the 3d$_{5/2}$ and 3d$_{3/2}$ respectively. These peaks signify the presence of iodine in the 3$^-$ (I^{3-}) oxidation state in the MAPI perovskite films. Fig. 4d shows the high-resolution spectrum of Pb 4f, where the peaks at 138.4 eV and 143.6 eV are attributed to the 4f$_{7/2}$ and 4f$_{5/2}$, respectively, which are signature peaks of the 2$^+$ oxidation state of Pb (Pb^{2+}).[26] Finally, Fig. 4e shows the high-resolution spectrum of N 1s and shows a high intense peak at low binding energy and the shoulder peak shifted to higher binding energies. The peak at 400 eV is associated with nitrogen singly bonded to carbon (–N–H) and the peak at 402 eV corresponds to the N–H3 singly bonded to the carbon in the MAPI perovskite

phase, with these results well matching with the reported literature.[24–26]

Photoexcited carrier behaviour was investigated using steady-state photoluminescence (PL) spectroscopy and the results are shown in Fig. 5a. It can be observed that all the perovskite thin-films showed prominent PL emission in the 776 nm wavelength region and these results are in good agreement with the UV absorbance data. The peak intensity of MAPI_MACl_1 is found to the very high and is four times higher than that of MAPI_120 °C, indicating the high crystal quality, in agreement with the XRD results and suppressed non-radiative recombination in the perovskite thin-films.[20,22] However, the PL peak intensity is gradually decreasing with the increase of the concentration of MACl. The excess amount of MACl leads to shrinkage in the perovskite crystals resulting in reduced grain size as observed from the SEM analysis. The reduced grain size leads to the creation of surface defects on the thin-films. These surface defects may be responsible for the increase in the non-radiative recombination resulting in the reduced PL peak intensity while increasing the concentration of MACl in the MAPI perovskite samples.[23] These results were further supported by the time-resolved photoluminescence (TRPL) decay measurements and are shown in Fig. 5b. These curves are fitted with the biexponential function (eqn (1)) containing both τ_1 and τ_2, indicating fast and slow decay lifetimes, respectively, where τ_1 and τ_2 are the PL decay times and A_1 and A_2 are the amplitudes.[23,27] The fast decay component τ_1 indicates charge carrier quenching at the interface and nonradiative recombination caused by charge trapping defects and the slow decay component τ_2 represents the bulk recombination of charge carriers.[28] Table S1 (ESI†) shows the charge carrier lifetime of all the perovskite thin-films. The τ_1 value of MAPI_MACl_1 was calculated to be 9.6 ns, which is higher than that of MAPI_120 °C (5.4 ns) indicating that MAPI_MACl_1 has minor surface defects resulting in the reduced nonradiative recombination, which is confirmed by surface morphology observed from the SEM analysis. The higher τ_2 value of
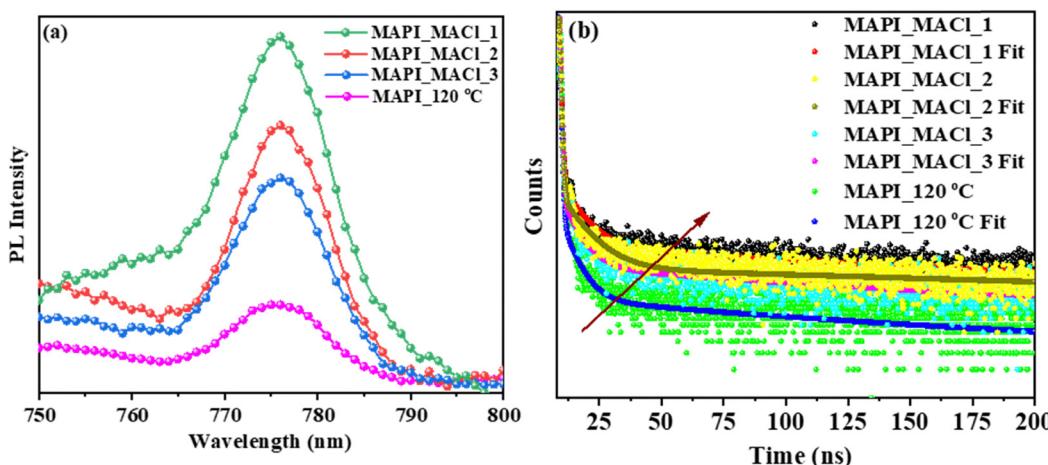
Fig. 5 (a) Steady state photoluminescence and (b) time resolved photoluminescence spectra of all the prepared perovskite thin-films. For PL, 565 nm excitation was used and a 390 nm nano-LED is used as an excitation source for TRPL measurements.

MAPI_MACl_1 indicates that the recombination in the bulk perovskite thin-film is also efficiently reduced.[23]

$$y = 1 + A_1 \exp\left(-\frac{x}{\tau_1}\right) + A_2 \exp\left(-\frac{x}{\tau_2}\right) \tag{1}$$

The photovoltaic performance of MACl-modified MAPI perovskite solar cells was fabricated with a carbon-based HTL-free device architecture (Fig. 6a) under ambient conditions with relative humidity around (50–60%) at room temperature. The solar cell J–V results are shown in Fig. 6b. The power conversion efficiency of our champion device (MAPI_MACl_1) is 7.11% with V_{oc} of 0.98 V and the I_{sc} is 11.03 mA cm^{-2} which is much higher than that of pristine MAPI_120 °C of 5.27% (V_{oc}: 1.0 V and I_{sc}: 8.95). All the solar cell parameters are summarized in Table 1. The FF of our champion device MAPI_MACl_1 of $\sim$65.86% is higher as compared with all the other devices due to the better charge transport at the interfaces.

All the devices showed a hysteresis effect, which is due to the weak interaction between the two layers in the perovskites solar cell resulting in defect generation (Fig. S4, ESI†). These defects are responsible for the increase in the hysteresis in the perovskite solar cells. There are different ways to reduce the hysteresis in the perovskite solar cells, such as improving the charge transporting ability via optimizing the charge transport layers, stabilizing perovskite materials and finding more

Table 1 Photovoltaic performance of all the fabricated devices

Sample	V_{oc}	I_{sc}	FF	PCE
MAPI_120 °C (RS)	1.01	8.95	58.82	5.27
MAPI_120 °C (FS)	1.00	8.98	52.31	4.70
MAPI_MACl_1 (RS)	0.98	11.03	65.86	7.11
MAPI_MACl_1 (FS)	0.98	11.06	57.02	6.18
MAPI_MACl_2 (RS)	0.96	11.02	59.29	6.27
MAPI_MACl_2 (FS)	0.96	11.05	53.61	5.69
MAPI_MACl_3 (RS)	1.00	10.17	52.22	5.31
MAPI_MACl_3 (FS)	1.00	10.27	46.41	4.77

suitable materials and finally, reducing the traps via optimizing the interfaces between the perovskite and charge transport layers.[29] In addition, we have done a stability study of the fabricated perovskite solar cells (Fig. 7). The device showed high stability over the period of 10 days stored under ambient conditions while retaining 80% of its initial efficiency. Whereas the pristine device showed a PCE of 5.27% and decreased $\sim$50% of its initial efficiency within 5 days. The enhanced photovoltaic performance of MAPI_MACl_1 is due to the reduced recombination of photogenerated charge carriers. The recombination behaviour of charge carriers was further investigated by using electrochemical impedance spectroscopy (EIS). The EIS measurements were done for all the fabricated devices and the results are shown in Fig. 6d. The MAPI_MACl_1 device shows high recombination resistance as compared to
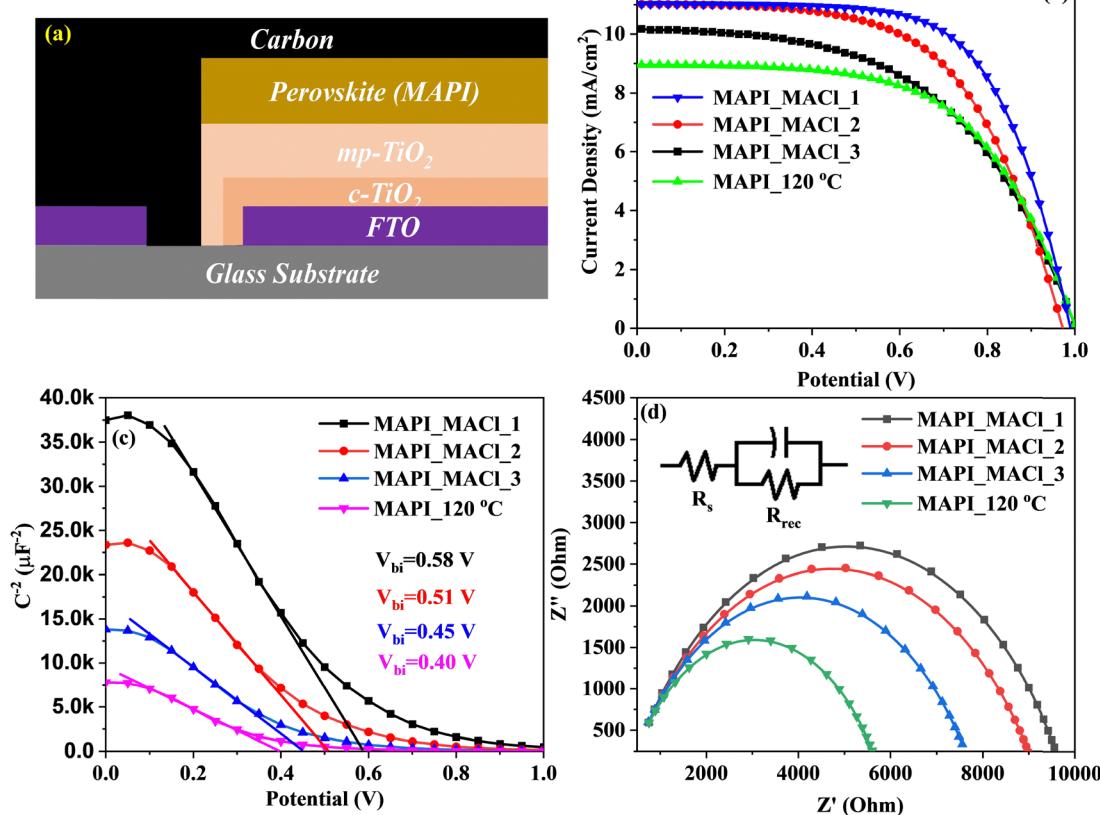

Fig. 6 (a) Schematic representation of the perovskite solar cell device architecture, (b) J–V characteristics of all the prepared devices, (c) Mott–Schottky plots of the prepared perovskite solar cell devices and (d) electrochemical impedance spectroscopy of all the fabricated devices (solid lines: measured values, symbols: fitted values) and the equivalent circuit diagram provided in the inset.
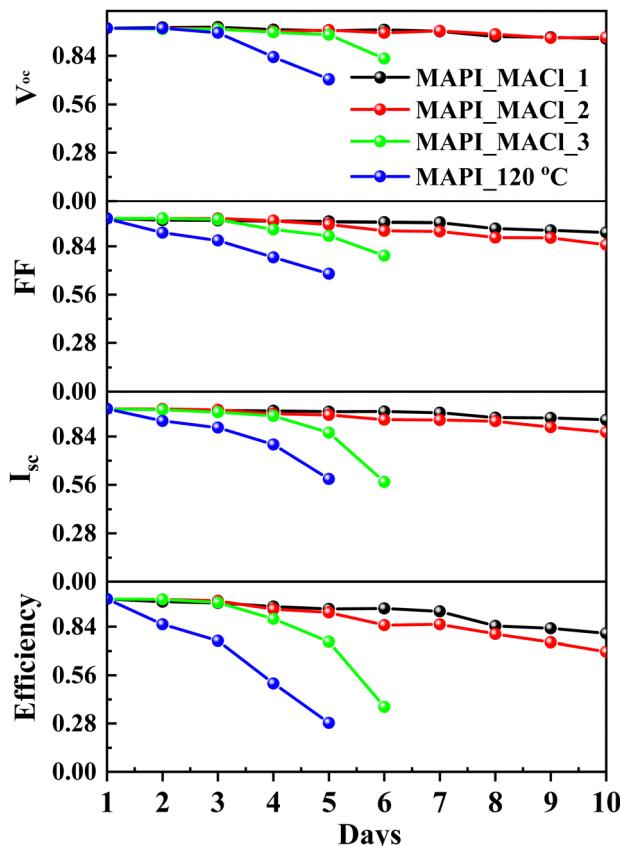
Fig. 7 Stability of the fabricated perovskite solar cells stored under ambient conditions over 10 days (normalized V_{oc}, FF, I_{sc} and PCE).

the other devices, which is attributed to the clean interface between the perovskite and other charge transport layers which is due to the incorporation of MACl.[30] Furthermore, to understand the interface contact between the perovskite/ETL and perovskite/carbon we conducted Mott–Schottky measurements for the fabricated devices. The built-in potential (V_{bi}) was obtained by fitting the linear region of the plot, as shown in Fig. 6c. It was observed that the device MAPI_MACl_1 shows a higher V_{bi} (0.58 V) as compared with the rest of the devices. This indicates that the larger V_{bi} not only suppresses the reverse transport of photogenerated charge carriers at the interface but also enhances the charge separation. That corroborates with the results obtained in impedance spectroscopy.[31] Typically, to attain high power conversion efficiency in the solar cell, the series resistance (R_s) should be low and the shunt resistance (R_{sh}) should be high. If the R_s is high, electrons cannot move freely along the circuit, and if the R_{sh} is low, leakage current will occur, which results in poor performance for the solar cell device. Fig. S5(a and b) (ESI†) shows the shunt and series resistance for all the perovskite solar cells and the values are summarized in Table S2 (ESI†). Fig. S5c (ESI†) shows the equivalent circuit diagram of the perovskite solar cell device. Interestingly, it is observed form Fig. S5(a and b) (ESI†) that the values for R_{sh} are higher ($\sim 5882\ \Omega$), whereas R_s ($\sim 20.80\ \Omega$) is lower for the MAPI_MACl_1 device indicating the better charge transport at both the interfaces between the perovskite and

carbon and the perovskite and ETL. EIS analysis also corroborates with the above studies that when the recombination resistance was observed to be higher it facilitates the lower charge recombination at the interface resulting in a high power conversion efficiency.[32] As previously discussed, MACl regulates the surface morphology of the perovskite thin-films by increasing the grain size in the order of 2, and MACl induces the room temperature formation of phase pure perovskite thin-films resulting in the high photovoltaic performance of the MACl-modified MAPI perovskite thin-films under ambient conditions.

Conclusions

In conclusion, we have demonstrated the HTL-free carbon-based perovskite solar cell device architecture fabricated under ambient conditions at room temperature. The MACl-modified perovskite solar cell devices showed enhanced power conversion efficiency of 7.11% with high stability over a period of 10 days stored under ambient atmosphere and retained 80% of their initial efficiency. This enhanced performance is due to the incorporation of MACl into the MAPI perovskite material. Which induces the room temperature formation of the phase pure semiconductor grade perovskite confirmed by XRD analysis. MACl modified films showed improved surface morphology with increased grain size on the order of 2 times as compared with the pristine one, which was confirmed by the SEM results. The enhanced optoelectronic properties of the MACl-modified films were studied by using UV-Vis, PL and lifetime analysis. The target films showed the enhanced optoelectronic properties, such as high absorption in the visible region, and showed enhanced PL emission, which indicated reduction in the non-radiative recombination. Furthermore, these results were supported by electrochemical impedance spectroscopy, which confirms the increased recombination resistance for the MACl added perovskite solar cells. This indicates improved charge carrier mobility in the device resulting in the high power conversion efficiency. This device architecture may be further used to fabricate stable ambient processed perovskite solar cells on a large scale to make them commercially viable.

Author contributions

Pardhasaradhi Nandigana: conceptualization, methodology, data generation, data curation and writing original draft. Bhavadarini S: synthesis of materials and characterization. Sriram P: original draft correction. Sujatha D: carbon paste preparation. Imthiaz and Ram Prasanth R: literature survey and characterization and plotting. Subhendu K. Panda: supervision, investigation, editing final draft.

Conflicts of interest

There are no conflicts to declare.

Acknowledgements

References

1 D. Weber, *Z. Naturforsch., B: J. Chem. Sci.*, 1978, **33**, 1443–1445.

2 C. Wehrenfennig, G. E. Eperon, M. B. Johnston, H. J. Snaith and L. M. Herz, *Adv. Mater.*, 2014, **26**, 1584–1589.

3 Y. Zhao and K. Zhu, *Chem. Soc. Rev.*, 2016, **45**, 655–689.

4 T. Jesper Jacobsson, J. P. Correa-Baena, M. Pazoki, M. Saliba, K. Schenk, M. Grätzel and A. Hagfeldt, *Energy Environ. Sci.*, 2016, **9**, 1706–1724.

5 A. Kojima, K. Teshima, Y. Shirai and T. Miyasaka, *J. Am. Chem. Soc.*, 2009, **131**, 6050–6051.

6 H. S. Kim, C. R. Lee, J. H. Im, K. B. Lee, T. Moehl, A. Marchioro, S. J. Moon, R. Humphry-Baker, J. H. Yum, J. E. Moser, M. Grätzel and N. G. Park, *Sci. Rep.*, 2012, **2**, 1–7.

7 https://www.nrel.gov/pv/cell-efficiency.html.

8 W. J. Yin, Y. Yan and S. H. Wei, *J. Phys. Chem. Lett.*, 2014, **5**, 3625–3631.

9 D. Liu, C. Yang, M. Bates and R. R. Lunt, *iScience*, 2018, **6**, 272–279.

10 M. Bari, H. Wu, A. A. Bokov, R. F. Ali, H. N. Tailor, B. D. Gates and Z. G. Ye, *CrystEngComm*, 2021, **23**, 3326–3339.

11 L. Zhang, C. Zuo and L. Ding, *J. Semicond.*, 2021, **42**, 72201.

12 Z. Yang, J. Pan, Y. Liang, Q. Li and D. Xu, *Small*, 2018, **14**, 1802240.

13 M. Liu, Z. Chen, Q. Xue, S. H. Cheung, S. K. So, H. L. Yip and Y. Cao, *J. Mater. Chem. A*, 2018, **6**, 16347–16354.

14 B. Yang, C. C. Brown, J. Huang, L. Collins, X. Sang, R. R. Unocic, S. Jesse, S. V. Kalinin, A. Belianinov, J. Jakowski, D. B. Geohegan, B. G. Sumpter, K. Xiao and O. S. Ovchinnikova, *Adv. Funct. Mater.*, 2017, **27**, 1700749.

15 Y. Zhao and K. Zhu, *J. Phys. Chem. C*, 2014, **118**, 9412–9418.

16 F. Xu, T. Zhang, G. Li and Y. Zhao, *ChemSusChem*, 2017, **10**, 2365–2369.

17 H. Tsai, W. Nie, P. Cheruku, N. H. MacK, P. Xu, G. Gupta, A. D. Mohite and H. L. Wang, *Chem. Mater.*, 2015, **27**, 5570–5576.

18 P. Docampo, F. C. Hanusch, S. D. Stranks, M. Döblinger, J. M. Feckl, M. Ehrensperger, N. K. Minar, M. B. Johnston, H. J. Snaith and T. Bein, *Adv. Energy Mater.*, 2014, **4**, 1–6.

19 Q. Chen, H. Zhou, Y. Fang, A. Z. Stieg, T. Bin Song, H. H. Wang, X. Xu, Y. Liu, S. Lu, J. You, P. Sun, J. McKay, M. S. Goorsky and Y. Yang, *Nat. Commun.*, 2015, **6** 1–9.

20 M. Kim, G. H. Kim, T. K. Lee, I. W. Choi, H. W. Choi, Y. Jo, Y. J. Yoon, J. W. Kim, J. Lee, D. Huh, H. Lee, S. K. Kwak, J. Y. Kim and D. S. Kim, *Joule*, 2019, **3**, 2179–2192.

21 X. Guo, C. McCleese, C. Kolodziej, A. C. S. Samia, Y. Zhao and C. Burda, *Dalton Trans.*, 2016, **45**, 3806–3813.

22 L. Bi, Q. Fu, Z. Zeng, Y. Wang, F. R. Lin, Y. Cheng, H. L. Yip, S. W. Tsang and A. K. Y. Jen, *J. Am. Chem. Soc.*, 2023, **145**, 5920–5929.

23 D. Liu, C. Li, C. Zhang, Z. Wang, H. Zhang, J. Tian and S. Pang, *RSC Adv.*, 2017, **7**, 51944–51949.

24 C. Rocks, V. Svrcek, T. Velusamy, M. Macias-Montero, P. Maguire and D. Mariotti, *Nano Energy*, 2018, **50**, 245–255.

25 C. Rocks, V. Svrcek, P. Maguire and D. Mariotti, *J. Mater. Chem. C*, 2017, **5**, 902–916.

26 G. Rajendra Kumar, A. Dennyson Savariraj, S. N. Karthick, S. Selvam, B. Balamuralitharan, H. J. Kim, K. K. Viswanathan, M. Vijaykumar and K. Prabakar, *Phys. Chem. Chem. Phys.*, 2016, **18**, 7284–7292.

27 S. Pari, P. Nandigana and S. K. Panda, *ACS Appl. Opt. Mater.*, 2023, **1**, 802–809.

28 E. Khorshidi, B. Rezaei, D. Blätte, A. Buyruk, M. A. Reus, J. Hanisch, B. Böller, P. Müller-Buschbaum and T. Ameri, *Sol. RRL*, 2022, **6**, 2200023.

29 P. Liu, W. Wang, S. Liu, H. Yang and Z. Shao, *Adv. Energy Mater.*, 2019, **9**, 1803017.

30 Y. Yang, K. Ri, A. Mei, L. Liu, M. Hu, T. Liu, X. Li and H. Han, *J. Mater. Chem. A*, 2015, **3**, 9103–9107.

31 Q. Xiong, L. Yang, Q. Zhou, T. Wu, C.-L. Mai, Z. Wang, S. Wu, X. Li and P. Gao, *ACS Appl. Mater. Interfaces*, 2020, **12**, 46306–46316.

32 D. I. Kim, J. W. Lee, R. H. Jeong and J.-H. Boo, *Sci. Rep.*, 2022, **12**, 697.